THE JOURNAL OF PHYSICAL CHEMISTRY C
A JOURNAL OF THE AMERICAN CHEMICAL SOCIETY

pubs.acs.org/JPCC

Article

Interplay between Electrostatic Properties of Molecular Adducts and Their Positions at Carbon Nanotubes

Braden M. Weight, Brendan J. Gifford, Sergei Tretiak, and Svetlana Kilina*

Cite This: *J. Phys. Chem. C* 2021, 125, 4785–4793

Read Online

ACCESS | Metrics & More | Article Recommendations | Supporting Information

ABSTRACT: Formation of the sp^3-defect due to covalent functionalization of a single-walled carbon nanotube (SWCNT) results in a new red-shifted emissive excitons. Using density functional theory, we study the impact of the intrinsic molecular dipole moments and the local charges induced by various molecular adducts on the energy and localization properties of the optically active defect-based exciton in a (10,5) SWCNT. The interplay of two effects plays a role in the localization of the exciton and, therefore, its red shift, but at different scales: The source of the leading order contribution is the defect conformation, resulting in the red shift of the defect-associated exciton with respect to the E_{11} band of the pristine SWCNT on the order of ∼100 meV, while the individual dipoles and polarization properties of molecular adducts lead to significantly smaller red shifts on the order of ∼10 meV. While the species-dependent trends in defect-induced charges do not directly correlate to the exciton red shift, the charge at the sp^3-defect exhibits a distinct behavior between *ortho*- and *para*-defect configurations and is relevant to the chemical reactivity of the defect position depending on the adduct type. Overall, our computational results may be helpful for diverse synthetic strategies to fine-tune emission of SWCNTs toward desired applications.

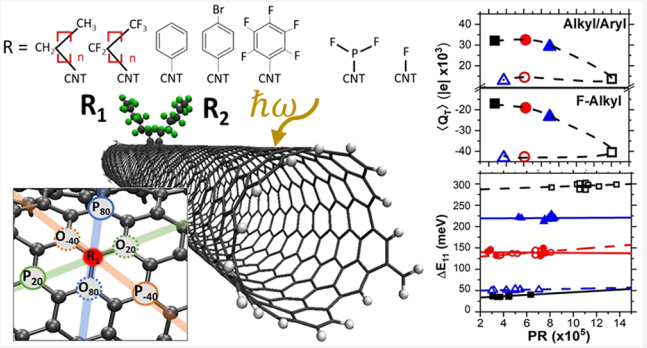

1. INTRODUCTION

Single-walled carbon nanotubes (SWCNTs) exhibit electronic and optical properties intrinsic to their structural features, including their diameter and chiral angles, which make them promising materials for applications in electronics, sensors, and photovoltaics.[1−8] In addition, the photophysical properties of SWCNTs can be modified by covalently binding small organic molecules to the SWCNT surface. Such functionalization changes the sp^2-hybridized carbon atom of the nanotube lattice to sp^3-hybridized by bonding with a pair of functional groups to a single carbon ring of the SWCNT.[9,10] Formation of the sp^3-defect results in new optically active transitions, E_{11}*, which are red-shifted from the main excitonic band, E_{11}.[3,11] In contrast to the lowest energy transitions of the pristine SWCNTs, the lowest energy defect-associated transitions are optically active, enhancing photoluminescence with quantum yields up to 30%.[12−14] The precise energy of the defect-associated transitions for a given chirality of a SWCNT has been found to be dependent on the topological characteristics of the defect on the nanotube surface.[9,13] The inducting ability of the molecular adduct has been also shown to impact the emission energy.[15] These dependences provide chemical tools for fine-tuning emission features targeting a specific application. For instance, aryl-functionalized SWCNTs have demonstrated unique room-temperature single-photon emission extending to telecom wavelengths suitable for quantum communication applications.[16−19]

While tuning of emission energies and their quantum yields is made possible through functionalization of SWCNTs with different chemical adducts,[13,20−24] the chemical effects responsible for the red shift and their dependence on the type of the functional group are not completely understood. The magnitude of red shifts has been attributed to inductive effects in the functional group, with an increasing red shift of E_{11}* with a stronger electron-withdrawing group.[15,25] However, calculations based on Density Functional theory (DFT) demonstrate that one or two halide substitutions in the aryl adduct has negligible effect on the lowest transition E_{11}*, despite increased dipole moment of the defect group.[3,10,12] On the other hand, it was shown that the dipole moment of the molecular adduct modifies the spatially dependent dielectric function of the functionalized SWCNT, which should affect the lowest energy exciton.[10,26]

Here, we have performed an extensive computational study aiming to clarify how the difference in the dipole moments of functional groups affects the defect-associated optical transition

Received: November 10, 2020
Revised: January 21, 2021
Published: February 22, 2021

https://dx.doi.org/10.1021/acs.jpcc.0c10157
J. Phys. Chem. C 2021, 125, 4785−4793

in SWCNTs. Applying time-dependent DFT (TD-DFT), we have found that the localization of exciton density near and on the chemical defect is greatly affected by two identical highly polar species bound to the same carbon ring at the surface of a (10,5) SWCNT, which results in the largest red shift of the E_{11}* exciton. In contrast, the defect comprising either polar or nonpolar species and a hydrogen atom exhibits much less exciton density at the molecular adduct, leading to smaller red shifts of E_{11}* transitions with respect to the parent E_{11} band. Nonetheless, neither the electrostatic dipole of the system nor the local charge induced by a molecular adduct at the nanotube atom is directly correlated with the red shift of the defect-associated exciton E_{11}* across all considered functional groups. Instead, the defect position at the nanotube surface plays the leading role in the localization and red shift of the trapped exciton.

2. METHODOLOGY AND COMPUTATIONAL DETAILS

2.1. Description of Considered Structures. A SWCNT of (10,5) chirality and ∼10 nm (3 primitive unit cells) in length was prepared using the Visual Molecular Dynamics (VMD) package.[27] Two dangling bonds on each end of the SWCNT were passivated with methylene groups, and the remaining dangling bonds were passivated with hydrogen atoms. This scheme has been shown to eliminate finite size effects and recover the intrinsic electronic structure of the infinite length system.[9,28] A functional group, R_1, is chosen from a class of alkyls, aryls, or non-carbon linkers (Figure 1a).

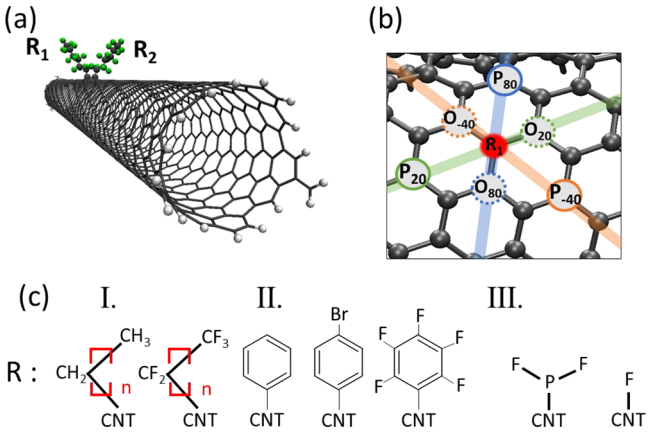

Figure 1. Structure of (10,5) SWCNT of 10.278 nm in length (3 primitive unit cells) with two functional groups R_1 and R_2 covalently attached to the same carbon ring of the SWCNT (a). The functional group R_2 can be placed in six unique positions with respect to R_1 (red circle): Three *ortho* (dashed circles) and three *para* (solid circles) (b). The functional groups are chosen from three classes of radicals: fully fluorinated and non-fluorinated alkyls with chain lengths $n \in \{1, 2, 6\}$ (Class I), phenyl, *p*-bromophenyl, and pentafluorophenyl (Class II), and fluorine and difluorophosphine (Class III) (c). The second functional group, R_2, is either the same as the first group ($2R_1$ structures) or hydrogen (R_1/H structures).

For alkyl groups with various chain lengths and dipole moments, we consider C_nH_{2n+1} and C_nF_{2n+1} (Class I), where n = 1, 2, or 6. Aryl groups are represented by C_6H_5, C_6H_4Br, and C_6F_5 (Class II). For the non-carbon groups, we explore F and PF_2 groups (Class III).

Placing a single molecular adduct on the surface of the nanotube creates an open-shell system that is highly reactive. As such, a second species, R_2, (an auxiliary group) is added in the vicinity of the first addition, so that both R_1 and R_2 adducts form a single sp^3-defect at the tube surface.[3,29] Two schemes with different auxiliary groups are studied here: one where both substituents are the same (called "R_1/R_1" or "$2R_1$") and another with a hydrogen atom as the auxiliary group (called "R_1/H"). In previous studies, it has been shown that six nearest neighbor positions (*ortho* and *para*) are available to place this auxiliary group to produce emissive (bright) defect-associated transitions.[3,9,13,29] This allows for three distinct *ortho*- and three distinct *para*-functionalization schemes. We utilize the notation previously established for defect positions, as illustrated in Figure 1b, where each *ortho* and *para* position is denoted by their approximate angle between R_1, R_2, and the nanotube axis.[30] Note, the exact values of these angles for the (10,5) SWCNT are 19.1°, 79.1°, and −40.9°, which are rounded to 20°, 80°, and −40°, respectively. Due to the absence of a resonance structure with charge in the *meta* position, placing an auxiliary group there generates a synthetically nonrelevant structure and is therefore not considered in this study. In light of recent work investigating densely packed, interacting defects on the SWCNT surface, we emphasize that we are working in the noninteracting limit (i.e., sparsely functionalized at low concentrations of reagent), where the nearest defect may be more than ∼100 nm away, on average, much larger than the native exciton size of ∼10 nm.[31,32]

2.2. Ground and Excited State Calculations. All calculations were performed using the Gaussian 16 rev. B.01 package.[33] Geometries were preoptimized using the semi-empirical Austin Model 1 (AM1).[34] DFT calculations were then performed using the long-range corrected hybrid functional CAM-B3LYP.[35] This functional has been shown to properly capture the localization of the electron density and the exciton to the region of the defect.[10] Basis set dependence on these systems was explored as an initial step: we examine three unique combinations of basis sets to yield computationally inexpensive, yet accurate, results.[36−42] One of three schemes was used for the basis set of the defect atoms: (i) all atoms calculated under STO-3G, (ii) only the halides calculated with 6-31G* with all other atoms calculated using STO-3G, and (iii) all atoms in the functional group plus tube carbon atoms adjacent to the defect calculated with 6-31G* with all other atoms calculated under STO-3G. For functional groups containing only carbon and hydrogen atoms (aryl and alkyl groups), an increase in the basis set from STO-3G to 6-31G* has a negligible effect on the electronic structure of the functionalized SWCNT (Figure 2a).

However, this is not the case for fluorinated alkyls. Using 6-31G* for fluorine atoms instead of STO-3G results in the larger difference (by ∼50 meV) in the HOMO-LUMO gap between the functionalized species and the pristine nanotube (ΔE_{HL}), compared to those calculated by STO-3G only, which is further increased when 6-31G* is used for the entire functional group according to the scheme (iii) (Figure 2a). Furthermore, the values of ΔE_{HL} calculated utilizing different basis sets are somewhat constant, regardless of the functional group or its position at the tube surface. Therefore, the energy gaps calculated by the reduced STO-3G basis set can be corrected as a constant energy shift, as has been described in our previous studies.[18] However, due to its substantially decreased HOMO-LUMO gaps for functionalization with

https://dx.doi.org/10.1021/acs.jpcc.0c10157
J. Phys. Chem. C 2021, 125, 4785−4793

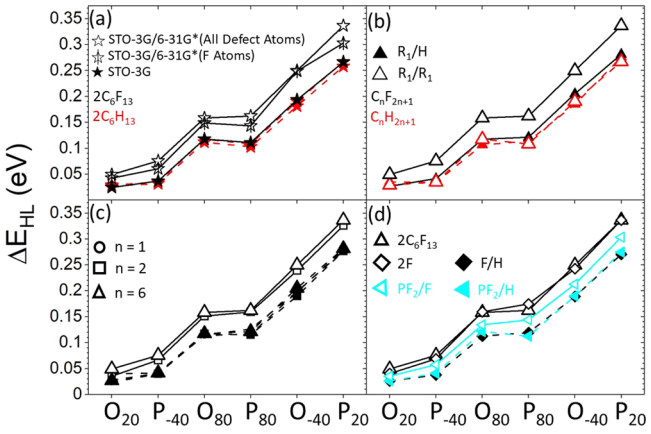

Figure 2. Difference in the HOMO-LUMO gap (ΔE_{HL}) between the pristine and functionalized (10.5) SWCNT as a function of the R_2 adduct position on the nanotube surface. (a) Comparison of ΔE_{HL} of structures with two fluorinated alkyl groups attached to the same carbon ring of the nanotube, $2C_6F_{13}$ (black), with those of non-fluorinated alkyls, $2C_6H_{13}$ (red), calculated by STO-3G (filled stars), and STO-3G/6-31G*, where the 6-31G* basis is used either for F atoms (slashed stars) or for the whole functional group, including the two carbons of the tube at the defect sites (empty stars). Empty and filled red stars overlap for the non-fluorinated alkyls pointing to the negligible effect of the basis set. This is not the case for fluorinated alkyls. (b) ΔE_{HL} comparison between structures with one alkyl and hydrogen, R_1/H (filled symbols and solid lines), and two identical alkyl groups, $2R_1 = R_1/R_1$ (empty symbols and dashed lines). The different number of carbons in alkyls (red) and fluorinated alkyls (black) corresponds to different symbols shown in the legend of the (c) panel. (c) Comparison of ΔE_{HL} for the fluorinated alkyls of various lengths and (d) for non-carbon groups of fluorine (empty and filled black diamonds) and difluorophosphine (empty and filled cyan triangles). In all cases, the O_{20} defect position results in the smallest ΔE_{HL}, whereas the P_{20} position leads to the largest ΔE_{HL}.

strongly polar groups, the scheme (iii) for the basis set has been chosen for all ground and excited state calculations.

The TD-DFT methodology was then used to obtain excited states[43−49] by applying the same density functional and basis sets as for the ground state calculations. The oscillator strengths were taken from the TD-DFT calculations, and, along with the transition energies, a continuous spectrum was constructed using the finite-width Gaussian curve, where the empirical width corresponds to a thermal broadening of 0.05 eV. To visualize the localization of the excitons in space, the Natural Transition Orbitals (NTOs) and the spatially resolved transition density were calculated.[50−52] To quantitatively analyze the localization of the transition density, we employed a participation ratio, PR_k, which is a heavily used technique for solid state physics applications in the analysis of defects and impurities.[53,54] The PR can be defined as

$$PR_k = \frac{\sum_i^N \rho(\boldsymbol{r}_i)^2}{[\sum_i^N \rho(\boldsymbol{r}_i)]^2} = \frac{\sum_i^N \psi(\boldsymbol{r}_i)^4}{[\sum_i^N \psi(\boldsymbol{r}_i)^2]^2} \quad (1)$$

where ρ is the electron density, ψ is a wave function (electron, hole, or quasi-particle), i is some spatial coordinate that uniquely defines each point in space with a total of N points, and k identifies a specific electronic state (e.g., Molecular Orbitals, MOs—for the ground state—or NTOs—for excitons). The PR_k value varies from 0 to 1. When PR_k approaches one, a small number of spatial points contribute more significantly than the other points, evidencing a localized nature of an exciton. Conversely, if PR_k is small, every point contributes nearly the same to the overall density, indicating in a completely delocalized exciton.

3. RESULTS AND DISCUSSION

The calculated HOMO-LUMO gap is 2.25 eV for the pristine (10,5) SWCNT, which is significantly blue-shifted compared to experimental values due to the lack of electron correlations for the ground state calculations and confinement effect of the finite-size (10 nm) nanotube model we use. However, this discrepancy does not affect the qualitative trends for comparing the electronic structure of pristine and functionalized SWCNTs, as investigated in our previous work.[55] Consistent with previous studies, functionalization results in destabilization of the HOMO and stabilization of the LUMO—both associated with the sp^3-defect site—leading to a decreased energy gap.[3,10,13] While the magnitude of this reduction is dependent on both the conformation and the chemical composition of the functional group, the topological position of the molecular adduct dominates (Figure 2b−d). In fact, changing the geometry of the defect results in a noticeable deviation between the energy gap of the pristine and functionalized SWCNTs (ΔE_{HL}) up to 350 meV. In contrast, the ΔE_{HL} value reaches no more than 100 meV, even for functional groups with highly electronegative fluorines (Figure 2b).

A steric effect between two long alkyl groups attached to the same carbon ring of the nanotube, $2C_6H_{13}$, negligibly impacts the electronic structure of the functionalized SWCNTs. As a result, the $2C_6H_{13}$ system exhibits similar values of ΔE_{HL} to the cases with a single alkyl and a hydrogen, C_6H_{13}/H, only demonstrating the dependence on the defect position (Figure 2b). This indicates that the impact of the second group on the electronic structure of the SWCNT is marginal for groups with weak electron-withdrawing ability, thereby validating the use of a hydrogen atom as the auxiliary group for modeling such systems. This is not the case for their fluorinated counterparts, where functionalization with two fluorinated chains, $2C_nF_{2n+1}$, results in a noticeable deviation of ΔE_{HL} from those of C_nF_{2n+1}/H structures (Figure 2c). A similar behavior is observed for two non-carbon adducts with a strong electron-withdrawing (F) or electron-donating (PF_2) character (Figure 2d). For all these cases, a strong electrostatic repulsion—strengthened by the inductive effect from an increased number of fluorine atoms in the alkyl chain—is expected to significantly affect the electron density of the SWCNTs, contributing to an observed reduction in the HOMO-LUMO gaps of the functionalized SWCNT, compared to its pristine counterpart. This gap energy reduction is the most pronounced for the structures with defects at the O_{-40} and P_{20} positions. In contrast, a dipole moment increase of a single functional group (C_nF_{2n+1}/H) results in much smaller (a few meV) deviations of ΔE_{HL} values between functional species (Figure 2c,d). Aryl groups act very similarly to C_nH_{2n+1}/H and C_nF_{2n+1}/H alkyls, showing an insignificant effect of the halide substituents on the values of ΔE_{HL}, Figure S1a in the Supporting Information (SI).

Having analyzed trends of the ground state energies, we next inspect the behavior of the excited state energies calculated with TD-DFT. The calculated E_{11} optical transition is at 1.52 eV for the pristine (10,5) SWCNT being closer to experiment owing to electronic correlations effects in TD-

https://dx.doi.org/10.1021/acs.jpcc.0c10157
J. Phys. Chem. C 2021, 125, 4785−4793

DFT. Similar trends for two functional groups ($2R_1$) versus one group (R_1/H) are observed for the excited states. Figure 3

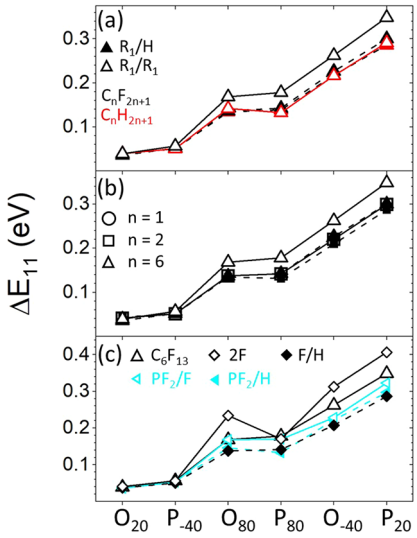

Figure 3. Red shift of the first absorption peak E_{11}^* of the functionalized SWCNT from E_{11} absorption band of the pristine SWCNT ($\Delta E_{11} = E_{11} - E_{11}^*$), as a function of the defect position. (a) Comparison between structures with two identical alkyl groups ($2R_1$ = R1/R_1, empty triangles and solid lines) and structures with one alkyl and hydrogen (R_1/H, filled triangles and dashed lines). (b) The effect of increasing the fluorinated alkyl chain length on the ΔE_{11} for $2R_1$ structures (empty triangles and solid lines) and R_1/H structures (filled triangles and dashed lines). (c) Comparison between non-carbon groups of fluorine (empty and filled black diamonds) and difluorophosphine (empty and filled cyan triangles) with the $2C_6F_{13}$ (empty black triangles).

shows the red shift of the defect-associated lowest optical transition, E_{11}^*, from the main absorption band, E_{11}, of the pristine nanotube: $\Delta E_{11} = E_{11} - E_{11}^*$. Similarities in the behavior of the ground and excited state electronic structures are rationalized by a predominant contribution of the HOMO-LUMO pair to the lowest energy excitonic wave function of SWCNT.[3,9,13] Therefore, the ΔE_{HL} at the ground state mainly follows the trends and characteristics of the low-lying excitons, ΔE_{11}, as evidenced by comparison of Figures 2 and 3. Overall, using two polar groups as adducts produces larger red shifts of the lowest excitons than substituting one with a hydrogen atom, which is the most pronounced for $2C_6F_{13}$ (Figure 3a,b) and 2F (Figure 3c) cases. These two structures provide the strongest red-shifted E_{11}^* transitions, well-distinct from E_{11}^* of other functional groups by about 60−100 meV at O_{-40} and P_{20} conformations (Figure S2 in SI), evidencing a dominant effect of the electrostatic interactions between neighboring functional groups on the lowest energy exciton.

Recent experimental data using high-resolution spectroscopy on a functionalized (6,5) SWCNT has detected a 19 meV difference between E_{11}^* excitons associated with defects due to functionalization by the 4-nitroaryl (strong electron-withdrawing group) versus 4-methoxyaryl (weaker electron-withdrawing group) and much smaller splitting of 4−6 meV between E_{11}^* of mixed defects when they are in very close proximity to each other.[56] Our calculations may explain these experimental trends. Assuming that similar types of molecular adducts can be attached to the same carbon ring of the nanotube, the species having strong electron-withdrawing abilities are expected to behave similarly to our 2F or $2C_6F_{13}$ model, resulting in a stronger red shift of the E_{11}^* exciton, compared to those of structures with weak electron-withdrawing characters (like our $2C_6H_{13}$ and aryl models). However, the mixture of two adducts with different electron-withdrawing abilities attached to the same carbon ring of the nanotube is expected to behave similarly to our F/H or C_6F_{13}/H models, resulting in insignificant E_{11}^* splitting between different species. Note that our calculations do not consider several sp^3-defects and interactions between them. Instead, two adduct molecules contribute to a single defect, while the difference in their interactions—due to variations in electrostatic properties of adducts—uniquely affects the exciton red shifts.

A recent experimental study reported an inductive effect of functional groups in connection to the defect-associated spectral features of SWCNTs.[25] A linear correlation between red shifts of emission energies and electron inductive ability of the functional group has been suggested. To get atomistic insights into this question, we provide the dependence of ΔE_{HL} and ΔE_{11} on the dipole moments of the SWCNT with various adducts to gauge the relationship between the electrostatic dipole and the defect-originated excitons in SWCNTs (Figure 4).

For a given type of the defect geometry, both ΔE_{HL} and ΔE_{11} tend to increase with the dipole moment of the functionalized (10,5). This trend is better pronounced for the most red-shifted geometries of O_{-40} and P_{20} (filled triangles and empty squares in Figure 4) and is very minor for O_{20} and P_{-40} defect positions (empty triangles and filled squares in Figure 4) having the least distorted electronic structure compared to the pristine SWCNT. We also note the lack of obvious correlations between the optical intensity of the lowest exciton and the system dipole moment (Figure S3).

For all defect positions, the increase in ΔE_{HL} and ΔE_{11} with the dipole moment of the system is very minor until the dipole reaches the value of 6 D. The trend is better pronounced after an inflection point at around 6 D, which mainly corresponds to structures having two adducts with strong electrostatic interactions, such as $2C_6F_{13}$, 2F, and PF_2/F (Figure 4). This trend is more conspicuous for the ground state ΔE_{HL} than the excited state transitions ΔE_{11} (compare Figure 4a to Figure 4b). For example, the exciton red shift of the 2F system (purple symbols in Figure 4b) is noticeably larger than that for the $2C_6F_{13}$ system (brown symbols in Figure 4b) that has a higher dipole moment compared to the 2F structure. The deviations in the trend point to the importance of direct interactions of the highly electronegative fluorines with the SWCNT rivaling the inductive capacity of the fluorinated alkyl group. This is expected to directly modify charge distributions in the region of the defect beyond dipole influence. As such, the dipole moment of the adduct alone does not seem to be a good indicator of the defect-originated exciton red shifts for most species studied here.

To investigate charge redistribution and charge-charge interactions between different functional groups, we examine the charge of the tube atom connected to the molecular adducts (Q_T), which is modified by hybridization, dipole, and inductive effects of the covalent attachment. Inductivity has been previously suggested to play a major role in resolving species-dependent shifts.[25,29] Here, we further explore this hypothesis, extending the studies to multiple binding configurations, including $2R_1$ groups. Figure 5 demonstrates

https://dx.doi.org/10.1021/acs.jpcc.0c10157
J. Phys. Chem. C 2021, 125, 4785−4793

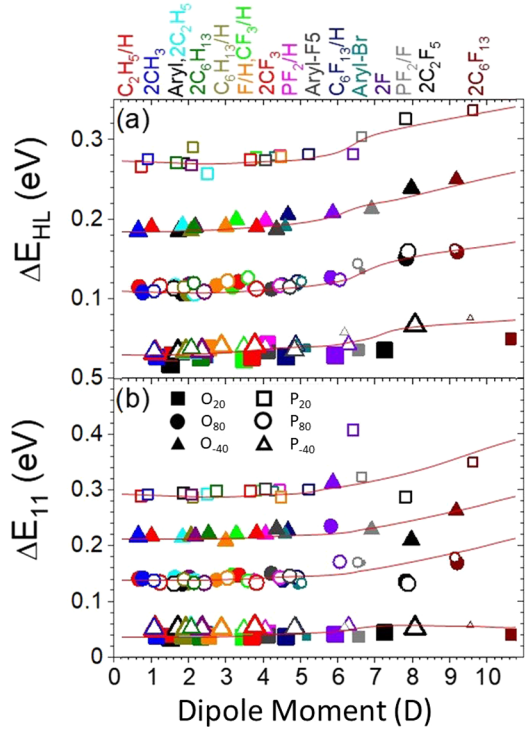

Figure 4. Dependence of the (a) ground state energy gap difference, ΔE_{HL}, and (b) excited state red shift, ΔE_{11}, on the electrostatic dipole moment of the functionalized SWCNT. Different colors of symbols represent different functional groups named at the top *X*-axis. The shape of symbols corresponds to the position of the defects at the SWCNT lattice. The size of the symbols corresponds to the oscillator strengths of E_{11}* transitions: the larger the symbol, the larger the oscillator strength. Both the ground state ΔE_{HL} and the excited state ΔE_{11} nearly monotonically increase with the dipole moment almost for all defect types and positions. This trend is less pronounced for ΔE_{11} of structures at O_{20} (filled squares) and P_{-40} (empty triangles) positions, which correspond to the brightest, delocalized, and least red-shifted E_{11}* excitons.

the correlations between the lowest energy exciton red shift ΔE_{11} and the local charges of the defect-connecting tube atom, Q_T, for each carbon-linking functional species and configuration we studied. Results for all functional groups, including 2F, F/H, PF_2/H, and PF_2/F, are shown in Figure S4. For the C_nH_{2n+1}, aryl, and F species, we observe that the charge induced on the nanotube atom has a positive sign, indicating that these molecular adducts work as electron-withdrawing groups (EWG) upon functionalization, with fluorines being the strongest EWG. In contrast, the fluorinated alkyl and PF_2 species have the opposite effect on Q_T as electron-donating groups (EDG), with PF_2 acting as the strongest EDG.

Near the zero-charge values, we note an interesting difference between the *ortho* and *para* positions (Figure 5). The alkyl/aryl EWG species with a positive Q_T exhibit the value of the charge 3−4 times smaller in the *para* than the *ortho* configurations. The reverse trend, although less pronounced, is true for the fluorinated alkyl EDG species inducing negative charge Q_T. For EWG alkyl/aryl species, this trend can be rationalized by a larger number of sp^2-hybridized nearest neighbor carbons in *para* (3), compared to *ortho* (2) configurations, which effectively minimizes the value of the positive Q_T in the *para*-defect. Significantly reduced Q_T in *para* positions of EWG can be also associated with a less reactive ability of *para* versus *ortho* positions. It was previously shown that there is a predominant selectivity for *ortho* binding configurations of aryl groups on the nanotube lattice, due to π−orbital misalignment enforced at the *ortho*-defect, making it highly reactive.[3,29,30] However, for the negative Q_T case in fluorinated alkyls, the reverse trend does not follow this argument, showing less distinction in the Q_T charge between the *para- and ortho*-defects. Overall, our data suggest that EWG functionalization leads to more localized positive charge at the defect in *ortho* attachment, whereas EDG functionalization more strongly localizes the negative charge in the *para*-defect. However, either the largest or the smallest positive or negative charges on the defect atom does not necessarily provide the largest red shift of the defect-associated excitation. For example, the red shift of the longest fluorinated alkyl chains, $2C_6F_{13}$, is the greatest in all defect positions but does not induce the largest negative charge in any configuration. This implies that there are additional factors determining the exciton red shift.

Consistent with previous reports,[3] there is a straightforward correlation between the exciton localization around the defect and its red shift: The higher the degree of exciton localization, the more the defect-associated exciton is red-shifted with respect to the E_{11} band (Table S1). Thus, regardless of the adduct species, a higher degree of localization of the transition charge density is seen near the defect in the O_{-40} and P_{20} positions, leading to the largest exciton red shift in comparison to the highly delocalized exciton of the O_{20} and P_{-40} positions, resulting in insignificant splitting between the defect-associated exciton and the E_{11} band (Table S1 and Figure S2). In our previous studies, we have provided physical interpretations of the difference in red shifts of optical features caused by the adduct positions: Similar to our finding here, strong red shifts in emission energies of certain defect geometries have been correlated to exciton localization, which is attributed to geometry-dependent variation in the nodes of the frontier orbitals.[57] In particular, when *ortho*-functionalization is performed along the less reactive axial bonds in the mod2 SWCNTs, such as O_{20} in (10,5) considered here, the resulting bond lies parallel to the nodes of the frontier orbitals and perturbations to the electronic structure are minimal.[57] Thus, the electronic structure and optical properties of the SWCNT functionalized along the axial O_{20} direction only marginally deviate from the pristine nanotube, resulting in the smallest red shifts. In contrast, the strongest red shift in mod2 nanotubes is the result of the defect along the highly reactive off-axial bonds (O_{-40} in (10,5) SWCNT), where the nodes of the frontier orbitals are bisected by the defect, resulting in strong exciton localization due to a significant disturbance to the orbital nodal structure in the vicinity of the defect.[57] Similar bisected node structures of the frontier orbitals in the P_{20} position also result in strong localization of the orbitals near the defect site, leading to the largest red shift of the lowest exciton.

This localization effect is analogous to exciton trapping by a quasi-one-dimensional potential energy well formed by the lattice defect.[12−14] The well depth and width are defined mostly by the geometric configuration of the defect associated with geometry-dependent variations in the nodes of the frontier orbitals[57] and to a weaker extent by the chemical species themselves. The latest is rationalized by the localization of the electron-hole density mainly on the defect, rather than on the functional group. However, the P_{20} configuration allows for some density to be drawn onto the anchoring atoms of the

https://dx.doi.org/10.1021/acs.jpcc.0c10157
J. Phys. Chem. C 2021, 125, 4785−4793

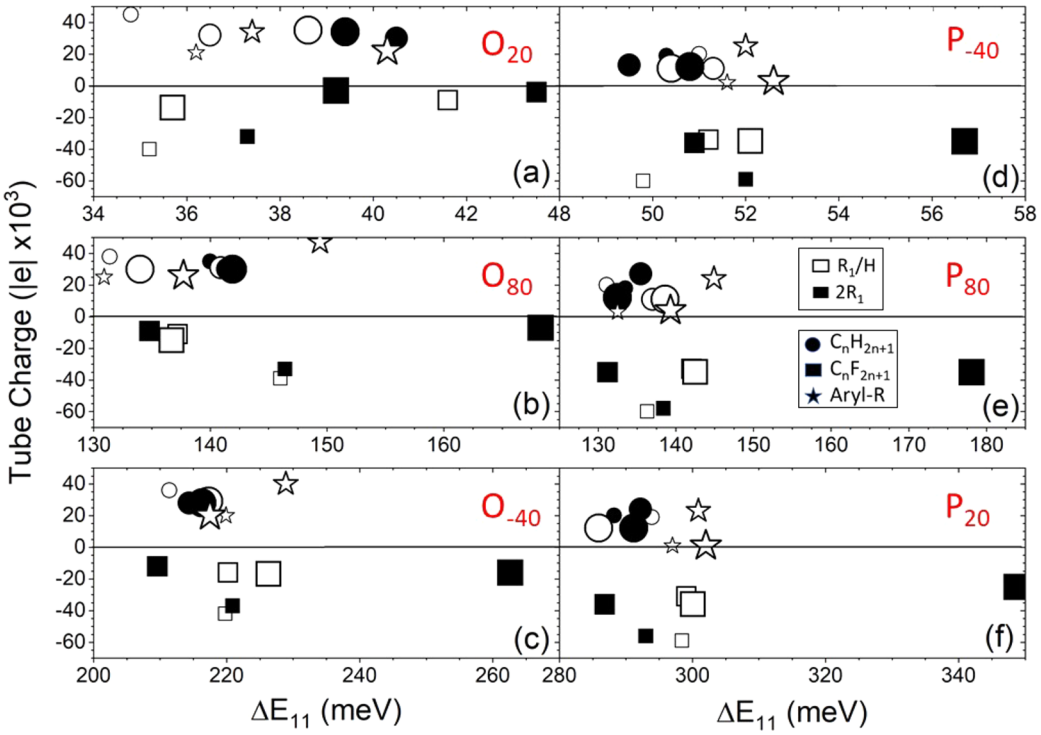

Figure 5. Charge on the nanotube carbon connected to the molecular adduct (Q_T) plotted as a function of the exciton red shift, $\Delta E_{11} = E_{11} - E_{11}^*$, for each configuration (a–f) and only carbon-linking functional groups. Increasing size of the symbol is correlated with increasing dipole moment and the chain length of the system.

functional group regardless of the species (Table S1). Similar behavior is observed for O_{-40}. This occurs even for a weakly EWG species such as non-fluorinated alkyls. This is due to the reduced width of the trapping well, which implies highly increased exciton localization in P_{20} and O_{-40} configurations, with some extension to the functional groups. Therefore, the exciton red shifts are more sensitive to the adduct species in P_{20} and O_{-40} configurations, compared to other defect positions (Figure 3).

We use PRs (as defined in eq 1) to provide a quantitative description of exciton localization in the considered systems, where larger PR values indicate increased localization. Two contrasting examples of such dependence can be seen in the top panel of Figure 6, where the NTOs corresponding to delocalized (left) and localized (right) excitons differ in PR by almost a factor of 10. Figure 6a shows the dependence of the averaged Q_T charge on the PR, where the charge values are averaged over all carbon-containing functional groups, separately presented for the EWG groups with the positive charge and EDG with the negative charge. For both EWG and EDG, the *para*-defects exhibit negligible changes in Q_T values on the exciton localization, with nearly neutral charge for EWG and the maximum negative values for EDG. In contrast, *ortho*-defects show a slight, but well-resolved, decrease in the positive charge with the exciton localization for EWG groups and increase in the negative charge for EDG groups with even stronger dependence (Figure 6a). These trends have potential importance for determining the reactive defect configuration implying that *ortho*-defects are likely more selective toward specific exciton energy, as it was previously suggested in literature reports.[3,29,30]

The dependence of the red shift of the defect-originated exciton on its localization for each defect configuration indicates a nearly ideal linear trend, when the values are averaged over all R_1/H species: The red shift of the defect-associated exciton strongly increases with its wave function localization as indicated by the PR (Figure 6b). More thorough analysis of this dependence focusing on individual contribution of each species is shown in Figure 6d and Figure S5.

Within each defect type, there is a weak increase of the exciton red shift with its PR, exhibiting more deviations for adducts at the defect positions with $\Delta E_{11} > 100$ meV. Comparison between the averaged data and individual ones shown in Figure 6b,d suggests the interplay of two effects playing a role in the localization of the excitonic state and, therefore, its red shift, but at different scales: defect configuration – ca. 100 meV, adduct species – ca. 10 meV.

As we have shown in Figure 4, most functional groups exhibit weak dependence of the exciton red shift on the dipole moment of the system, where only adducts with the largest dipoles cause significant effects. Figures 6c and S5b also demonstrate the minor dependence of the exciton localization on the dipole moment by showing the PR as a function of the dipole moment for each system. Within each defect configuration, on average, nearly linear dependence between the PR and dipole moments can be observed, although the values for each species are significantly scattered from the averaged line. While the exciton localization insignificantly affects the Q_T charge for *para*-defects (Figure 6a), the dipole moment of species at the *para* positions demonstrate much stronger dependence, compared to *ortho* positions (Figure 6c). The exception is O_{80} and P_{80} defects, which we single out as having the largest standard deviations from the linear trend for these cases, compared to other defects. In general, significant scattering of data in Figure 6c points to a stronger dependence of the dipole moment on the chemical composition of adducts,

https://dx.doi.org/10.1021/acs.jpcc.0c10157
J. Phys. Chem. C 2021, 125, 4785–4793

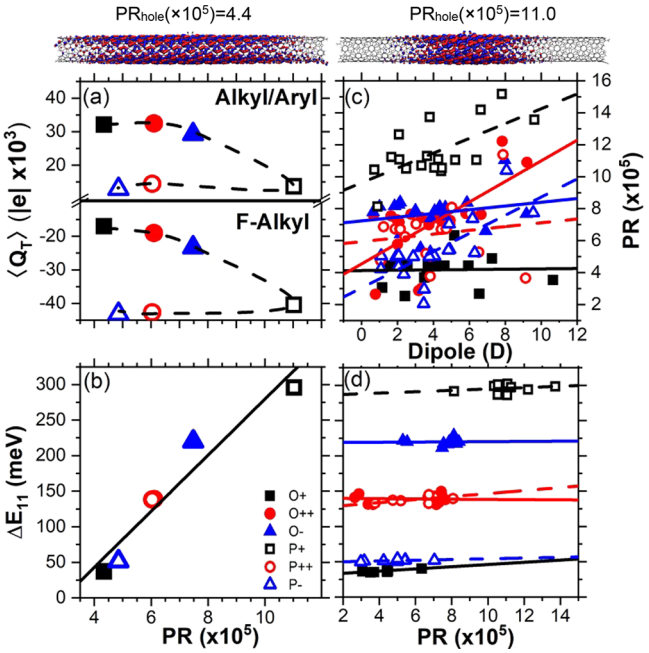

Figure 6. Correlation between individual electrostatic properties of molecular adducts and the participation ratio (PR) of functionalized (10,5) SWCNT. Two natural transition orbitals (NTOs) for the 2F O_{20} and P_{20} geometries corresponding to the hole with their associated PR value, depicting how exciton localization is quantified using the PR (top panel). (a) Charge on the nanotube atom connected to the chemical adduct (Q_T) as a function of the participation ratio. The positive-(negative-)charge panel is the average charge of the alkyl and aryl (fluorinated alkyl) species for all carbon-based adducts in each configuration, including both R_1/H and $2R_1$ systems. The points are connected with dashed lines for better visualization of the trend. (b) Red shift of the defect-originated exciton from the main E_{11} band ($\Delta E_{11} = E_{11} - E_{11}^*$) as a function of its participation ratio. The symbols represent an average over all R_1/H molecular adducts in a given defect configuration. (c) The dependence of the participation ratio on the dipole moment of the system for all considered functional groups. (d) The dependence of the red shift ΔE_{11} on the participation ratio for R_1/H molecular adducts in a given defect configuration. A linear fit is shown by a solid (*ortho*-defects) and dashed (*para*-defects) lines.

rather than the ability of the sp^3-defect to localize the exciton. This difference can be rationalized by polarization properties of the excited state due to the charge density redistribution upon excitation that compensates the effect of electrostatic charge distribution associated with the electrostatic dipole moment of the ground state.

4. CONCLUSIONS

Using DFT-based methodologies, we have investigated the effect of the intrinsic molecular dipole moments and the local charges induced by various molecular adducts on the energy and wave function localization properties of the optically active defect-associated excitons in a (10,5) functionalized SWCNT. Our results evidence that neither the dipole moment nor inductive features—including local charge on the SWCNT-defect interface—can serve as reliable descriptors of the energy splitting between the defect-associated exciton and the main E_{11} band of the SWCNTs. When considering the electrostatic dipole moment of the system, the overall trends are consistent with the expectation that the red shift of the defect-associated exciton increases with the dipole moment of the functionalized SWCNT, but exhibiting very weak dependence, except for significantly large values of the dipole moments (>6 D). Notably, such a large dipole moment of the system can be introduced only by two strong EWG or EDG, such as 2F or $2C_6F_{13}$ and PF_2/F attached to the same carbon ring of the nanotube. However, the effect of a single group—F/H, C_nF_{2n+1}/H, and PF_2/H—is nearly the same as for weak EWG or EDG groups, such as aryls and non-fluorinated alkyls. In addition, the dipole moment of the species poorly correlates with the exciton localization, while the latter exhibits a strong linear dependence on the red shifts of the defect-associated excitons. Our calculations demonstrate that the degree of localization of the defect-associated exciton, which can be measured using the participation ratio, is a suitable empirical parameter to determine the energy splitting between the defect-originated exciton and the E_{11} band in the covalently functionalized SWCNTs. However, no adduct-dependent parameter was found to strongly correlate with this variable.

The charge at the sp^3-defect shows a distinct behavior between *ortho*- and *para*-defect configurations, regardless of molecular adducts, and likely relevant to the chemical reactivity of the defect position. However, the species-dependent trends in charges induced by molecular adducts do not directly correlate to the exciton red shift across all considered functional groups. We explain such a weak dependence by the redistribution of the exciton density of the excited state that weakens the polarization effect of the electrostatic dipole moment of the ground state. This leads to the localization of the lowest energy exciton mainly around the sp^3-defect of the nanotube with a negligible extent of its density distributed to the anchoring atoms of the functional group. Therefore, the defect configuration plays the leading role in the red shift of the defect-associated exciton with respect to the E_{11} band of the pristine SWCNTs on the order of ca. 100 meV, while the polarization properties of molecular adducts lead to significantly smaller red shifts on the order of ca. 10 meV. In ref 57, it was shown that all investigated trends in electronic and optical properties relating to the defect configuration are similar for SWCNTs of the same mod(n-m,3). As such, we also can assume that all trends obtained for (10,5) can be generalized to other SWCNTs of mod2. These computational results may aid in finding improvements of synthetic protocols to achieve desired emission of functionalized SWCNTs.

■ ASSOCIATED CONTENT

Supporting Information

The Supporting Information is available free of charge at https://pubs.acs.org/doi/10.1021/acs.jpcc.0c10157.

Various additional plots to supplement most main figures, simulated absorption plots for comparing the effects of fluorination and Natural Transition Orbitals (NTOs) to showcase the size of the exciton and its locality to and on the defect, and tables of data for most of the necessary observables in this work, as there are many overlapping data points in the figures (PDF)

■ AUTHOR INFORMATION

Corresponding Author

Svetlana Kilina − *Department of Chemistry and Biochemistry, North Dakota State University, Fargo, North Dakota 58108, United States;* orcid.org/0000-0003-1350-2790; Email: Svetlana.kilina@ndsu.edu

https://dx.doi.org/10.1021/acs.jpcc.0c10157
J. Phys. Chem. C 2021, 125, 4785−4793

Authors

Braden M. Weight − *Department of Chemistry and Biochemistry, North Dakota State University, Fargo, North Dakota 58108, United States; Theoretical Division, Los Alamos National Laboratory, Los Alamos, New Mexico 87545, United States;* orcid.org/0000-0002-2441-3569

Brendan J. Gifford − *Theoretical Division, Center for Nonlinear Studies, and Center for Integrated Nanotechnologies, Materials Physics and Applications Division, Los Alamos National Laboratory, Los Alamos, New Mexico 87545, United States;* orcid.org/0000-0002-4116-711X

Sergei Tretiak − *Theoretical Division, Center for Nonlinear Studies, and Center for Integrated Nanotechnologies, Materials Physics and Applications Division, Los Alamos National Laboratory, Los Alamos, New Mexico 87545, United States;* orcid.org/0000-0001-5547-3647

Complete contact information is available at: https://pubs.acs.org/10.1021/acs.jpcc.0c10157

Notes

The authors declare no competing financial interest.

■ ACKNOWLEDGMENTS

S.K. and B.M.W. are thankful for the financial support of DOE EPSCoR: Building EPSCoR-State/National Laboratory Partnerships grant no. DE-SC0021287. For computational resources and administrative support, the authors thank the Center for Computationally Assisted Science and Technology (CCAST) at North Dakota State University and the National Energy Research Scientific Computing Center (NERSC) allocation award 86678, supported by the Office of Science of the DOE under contract no. DE-AC02-05CH11231. This work was performed in part at the Center for Integrated Nanotechnology (CINT), a U.S. Department of Energy and Office of Basic Energy Sciences user facility, and supported by the Los Alamos National Laboratory (LANL) Directed Research and Development funds (LDRD).

■ REFERENCES

(1) Baughman, R. H. Carbon Nanotubes–the Route Toward Applications. *Science* **2002**, *297* (5582), 787−792.

(2) Roslyak, O.; Cherqui, C.; Dunlap, D. H.; Piryatinski, A. Effect of Localized Surface-Plasmon Mode on Exciton Transport and Radiation Emission in Carbon Nanotubes. *J. Phys. Chem. B* **2014**, *118* (28), 8070−8080.

(3) Gifford, B. J.; Kilina, S.; Htoon, H.; Doorn, S. K.; Tretiak, S. Exciton Localization and Optical Emission in Aryl-Functionalized Carbon Nanotubes. *J. Phys. Chem. C* **2018**, *122* (3), 1828−1838.

(4) Ma, X.; Roslyak, O.; Wang, F.; Duque, J. G.; Piryatinski, A.; Doorn, S. K.; Htoon, H. Influence of Exciton Dimensionality on Spectral Diffusion of Single-Walled Carbon Nanotubes. *ACS Nano* **2014**, *8* (10), 10613−10620.

(5) Vialla, F.; Chassagneux, Y.; Ferreira, R.; Roquelet, C.; Diederichs, C.; Cassabois, G.; Roussignol, Ph.; Lauret, J. S.; Voisin, C. Unifying the Low-Temperature Photoluminescence Spectra of Carbon Nanotubes: The Role of Acoustic Phonon Confinement. *Phys. Rev. Lett.* **2014**, *113* (5), 057402.

(6) Jeantet, A.; Chassagneux, Y.; Raynaud, C.; Roussignol, Ph.; Lauret, J. S.; Besga, B.; Estève, J.; Reichel, J.; Voisin, C. Widely Tunable Single-Photon Source from a Carbon Nanotube in the Purcell Regime. *Phys. Rev. Lett.* **2016**, *116* (24), 247402.

(7) Legrand, D.; Roquelet, C.; Lanty, G.; Roussignol, Ph.; Lafosse, X.; Bouchoule, S.; Deleporte, E.; Voisin, C.; Lauret, J. S. Monolithic Microcavity with Carbon Nanotubes as Active Material. *Appl. Phys. Lett.* **2013**, *102* (15), 153102.

(8) Ardizzone, V.; Chassagneux, Y.; Vialla, F.; Delport, G.; Delcamp, C.; Belabas, N.; Deleporte, E.; Roussignol, Ph.; Robert-Philip, I.; Voisin, C.; et al. Strong Reduction of Exciton-Phonon Coupling in Single-Wall Carbon Nanotubes of High Crystalline Quality: Insight into Broadening Mechanisms and Exciton Localization. *Phys. Rev. B: Condens. Matter Mater. Phys.* **2015**, *91* (12), 121410.

(9) Kilina, S.; Ramirez, J.; Tretiak, S. Brightening of the Lowest Exciton in Carbon Nanotubes via Chemical Functionalization. *Nano Lett.* **2012**, *12* (5), 2306−2312.

(10) Ramirez, J.; Mayo, M. L.; Kilina, S.; Tretiak, S. Electronic Structure and Optical Spectra of Semiconducting Carbon Nanotubes Functionalized by Diazonium Salts. *Chem. Phys.* **2013**, *413*, 89−101.

(11) Bouilly, D.; Janssen, J. L.; Cabana, J.; Côté, M.; Martel, R. Graft-Induced Midgap States in Functionalized Carbon Nanotubes. *ACS Nano* **2015**, *9* (3), 2626−2634.

(12) Hartmann, N. F.; Yalcin, S. E.; Adamska, L.; Hároz, E. H.; Ma, X.; Tretiak, S.; Htoon, H.; Doorn, S. K. Photoluminescence Imaging of Solitary Dopant Sites in Covalently Doped Single-Wall Carbon Nanotubes. *Nanoscale* **2015**, *7* (48), 20521−20530.

(13) He, X.; Gifford, B. J.; Hartmann, N. F.; Ihly, R.; Ma, X.; Kilina, S. V.; Luo, Y.; Shayan, K.; Strauf, S.; Blackburn, J. L.; et al. Low-Temperature Single Carbon Nanotube Spectroscopy of Sp ^{3} Quantum Defects. *ACS Nano* **2017**, *11* (11), 10785−10796.

(14) Piao, Y.; Meany, B.; Powell, L. R.; Valley, N.; Kwon, H.; Schatz, G. C.; Wang, Y. Brightening of Carbon Nanotube Photoluminescence through the Incorporation of Sp 3 Defects. *Nat. Chem.* **2013**, *5* (10), 840−845.

(15) Shiraki, T.; Uchimura, S.; Shiraishi, T.; Onitsuka, H.; Nakashima, N. Near Infrared Photoluminescence Modulation by Defect Site Design Using Aryl Isomers in Locally Functionalized Single-Walled Carbon Nanotubes. *Chem. Commun.* **2017**, *53* (93), 12544−12547.

(16) Ma, X.; Hartmann, N. F.; Baldwin, J. K. S.; Doorn, S. K.; Htoon, H. Room-Temperature Single-Photon Generation from Solitary Dopants of Carbon Nanotubes. *Nat. Nanotechnol.* **2015**, *10* (8), 671−675.

(17) Kim, Y.; Goupalov, S. V.; Weight, B. M.; Gifford, B. J.; He, X.; Saha, A.; Kim, M.; Ao, G.; Wang, Y.; Zheng, M.; et al. Hidden Fine Structure of Quantum Defects Revealed by Single Carbon Nanotube Magneto-Photoluminescence. *ACS Nano* **2020**, *14* (3), 3451−3460.

(18) Gifford, B. J.; Kilina, S.; Htoon, H.; Doorn, S. K.; Tretiak, S. Controlling Defect-State Photophysics in Covalently Functionalized Single-Walled Carbon Nanotubes. *Acc. Chem. Res.* **2020**, *53* (9), 1791−1801.

(19) Saha, S.; Dinadayalane, T. C.; Murray, J. S.; Leszczynska, D.; Leszczynski, J. Surface Reactivity for Chlorination on Chlorinated (5,5) Armchair SWCNT: A Computational Approach. *J. Phys. Chem. C* **2012**, *116* (42), 22399−22410.

(20) Ghosh, S.; Bachilo, S. M.; Simonette, R. A.; Beckingham, K. M.; Weisman, R. B. Oxygen Doping Modifies Near-Infrared Band Gaps in Fluorescent Single-Walled Carbon Nanotubes. *Science* **2010**, *330* (6011), 1656−1659.

(21) Ma, X.; Adamska, L.; Yamaguchi, H.; Yalcin, S. E.; Tretiak, S.; Doorn, S. K.; Htoon, H. Electronic Structure and Chemical Nature of Oxygen Dopant States in Carbon Nanotubes. *ACS Nano* **2014**, *8* (10), 10782−10789.

(22) Miyauchi, Y.; Iwamura, M.; Mouri, S.; Kawazoe, T.; Ohtsu, M.; Matsuda, K. Brightening of Excitons in Carbon Nanotubes on Dimensionality Modification. *Nat. Photonics* **2013**, *7* (9), 715−719.

(23) Ma, X.; Baldwin, J. K. S.; Hartmann, N. F.; Doorn, S. K.; Htoon, H. Solid-State Approach for Fabrication of Photostable, Oxygen-Doped Carbon Nanotubes. *Adv. Funct. Mater.* **2015**, *25* (39), 6157−6164.

(24) Shiraki, T.; Shiraishi, T.; Juhász, G.; Nakashima, N. Emergence of New Red-Shifted Carbon Nanotube Photoluminescence Based on Proximal Doped-Site Design. *Sci. Rep.* **2016**, *6* (1), 28393.

(25) Kwon, H.; Furmanchuk, A.; Kim, M.; Meany, B.; Guo, Y.; Schatz, G. C.; Wang, Y. Molecularly Tunable Fluorescent Quantum Defects. *J. Am. Chem. Soc.* **2016**, *138* (21), 6878−6885.
(26) McMahon, J. M.; Gray, S. K.; Schatz, G. C. Optical Properties of Nanowire Dimers with a Spatially Nonlocal Dielectric Function. *Nano Lett.* **2010**, *10* (9), 3473−3481.
(27) Humphrey, W.; Dalke, A.; Schulten, K. VMD: Visual Molecular Dynamics. *J. Mol. Graphics* **1996**, *14* (1), 33−38.
(28) Sharma, A.; Gifford, B. J.; Kilina, S. Tip Functionalization of Finite Single-Walled Carbon Nanotubes and Its Impact on the Ground and Excited State Electronic Structure. *J. Phys. Chem. C* **2017**, *121* (15), 8601−8612.
(29) Gifford, B. J.; He, X.; Kim, M.; Kwon, H.; Saha, A.; Sifain, A. E.; Wang, Y.; Htoon, H.; Kilina, S.; Doorn, S. K.; et al. Optical Effects of Divalent Functionalization of Carbon Nanotubes. *Chem. Mater.* **2019**, *31* (17), 6950−6961.
(30) Saha, A.; Gifford, B. J.; He, X.; Ao, G.; Zheng, M.; Kataura, H.; Htoon, H.; Kilina, S.; Tretiak, S.; Doorn, S. K. Narrow-Band Single-Photon Emission through Selective Aryl Functionalization of Zigzag Carbon Nanotubes. *Nat. Chem.* **2018**, *10* (11), 1089−1095.
(31) Zheng, Y.; Bachilo, S. M.; Weisman, R. B. Photoexcited Aromatic Reactants Give Multicolor Carbon Nanotube Fluorescence from Quantum Defects. *ACS Nano* **2020**, *14* (1), 715−723.
(32) Zheng, Y.; Bachilo, S. M.; Weisman, R. B. Controlled Patterning of Carbon Nanotube Energy Levels by Covalent DNA Functionalization. *ACS Nano* **2019**, *13* (7), 8222−8228.
(33) Frisch, M. J.; Trucks, G. W.; Schlegel, H. B.; Scuseria, G. E.; Robb, M. A.; Cheeseman, J. R.; Scalmani, G.; Barone, V.; Petersson, G. A.; Nakatsuji, H.; et al. *Gaussian 16*, rev. B.01; Gaussian, Inc.: Wallingford, CT, 2016.
(34) Dewar, M. J. S.; Zoebisch, E. G.; Healy, E. F.; Stewart, J. J. P. Development and Use of Quantum Mechanical Molecular Models. 76. AM1: A New General Purpose Quantum Mechanical Molecular Model. *J. Am. Chem. Soc.* **1985**, *107* (13), 3902−3909.
(35) Yanai, T.; Tew, D. P.; Handy, N. C. A New Hybrid Exchange−Correlation Functional Using the Coulomb-Attenuating Method (CAM-B3LYP). *Chem. Phys. Lett.* **2004**, *393* (1), 51−57.
(36) Weigend, F.; Ahlrichs, R. Balanced Basis Sets of Split Valence, Triple Zeta Valence and Quadruple Zeta Valence Quality for H to Rn: Design and Assessment of Accuracy. *Phys. Chem. Chem. Phys.* **2005**, *7* (18), 3297−3305.
(37) Clark, T.; Chandrasekhar, J.; Spitznagel, G. W.; Schleyer, P. V. R. Efficient Diffuse Function-Augmented Basis Sets for Anion Calculations. III. The 3-21+G Basis Set for First-Row Elements, Li−F. *J. Comput. Chem.* **1983**, *4* (3), 294−301.
(38) Ditchfield, R.; Hehre, W. J.; Pople, J. A. Self-Consistent Molecular-Orbital Methods. IX. An Extended Gaussian-Type Basis for Molecular-Orbital Studies of Organic Molecules. *J. Chem. Phys.* **1971**, *54* (2), 724−728.
(39) Dobbs, K. D.; Hehre, W. J. Molecular Orbital Theory of the Properties of Inorganic and Organometallic Compounds. 6. Extended Basis Sets for Second-Row Transition Metals. *J. Comput. Chem.* **1987**, *8* (6), 880−893.
(40) Gill, P. M. W.; Johnson, B. G.; Pople, J. A.; Frisch, M. J. The Performance of the Becke—Lee—Yang—Parr (B—LYP) Density Functional Theory with Various Basis Sets. *Chem. Phys. Lett.* **1992**, *197* (4), 499−505.
(41) Collins, J. B.; von R. Schleyer, P.; Binkley, J. S.; Pople, J. A. Self-consistent Molecular Orbital Methods. XVII. Geometries and Binding Energies of Second-row Molecules. A Comparison of Three Basis Sets. *J. Chem. Phys.* **1976**, *64* (12), 5142−5151.
(42) Gordon, M. S.; Binkley, J. S.; Pople, J. A.; Pietro, W. J.; Hehre, W. J. Self-Consistent Molecular-Orbital Methods. 22. Small Split-Valence Basis Sets for Second-Row Elements. *J. Am. Chem. Soc.* **1982**, *104* (10), 2797−2803.
(43) Furche, F.; Ahlrichs, R. Adiabatic Time-Dependent Density Functional Methods for Excited State Properties. *J. Chem. Phys.* **2002**, *117* (16), 7433−7447.
(44) Adamo, C.; Jacquemin, D. The Calculations of Excited-State Properties with Time-Dependent Density Functional Theory. *Chem. Soc. Rev.* **2013**, *42* (3), 845−8.
(45) Badaeva, E.; Albert, V. V.; Kilina, S.; Koposov, A.; Sykora, M.; Tretiak, S. Effect of Deprotonation on Absorption and Emission Spectra of Ru(II)-Bpy Complexes Functionalized with Carboxyl Groups. *Phys. Chem. Chem. Phys.* **2010**, *12* (31), 8902−8913.
(46) Li, Y.; Dandu, N.; Liu, R.; Li, Z.; Kilina, S.; Sun, W. Effects of Extended π-Conjugation in Phenanthroline (N∧N) and Phenylpyridine (C∧N) Ligands on the Photophysics and Reverse Saturable Absorption of Cationic Heteroleptic Iridium(III) Complexes. *J. Phys. Chem. C* **2014**, *118* (12), 6372−6384.
(47) Stratmann, R. E.; Scuseria, G. E.; Frisch, M. J. An Efficient Implementation of Time-Dependent Density-Functional Theory for the Calculation of Excitation Energies of Large Molecules. *J. Chem. Phys.* **1998**, *109* (19), 8218−8224.
(48) Miller, J. B.; Dandu, N.; Velizhanin, K. A.; Anthony, R. J.; Kortshagen, U. R.; Kroll, D. M.; Kilina, S.; Hobbie, E. K. Enhanced Luminescent Stability through Particle Interactions in Silicon Nanocrystal Aggregates. *ACS Nano* **2015**, *9* (10), 9772−9782.
(49) Van Caillie, C.; Amos, R. D. Geometric Derivatives of Excitation Energies Using SCF and DFT. *Chem. Phys. Lett.* **1999**, *308* (3), 249−255.
(50) Martin, R. L. Natural Transition Orbitals. *J. Chem. Phys.* **2003**, *118* (11), 4775−4777.
(51) Luzanov, A. V.; Sukhorukov, A. A.; Umanskii, V. É. Application of Transition Density Matrix for Analysis of Excited States. *Theor. Exp. Chem.* **1976**, *10* (4), 354−361.
(52) Barone, V.; Peralta, J. E.; Wert, M.; Heyd, J.; Scuseria, G. E. Density Functional Theory Study of Optical Transitions in Semiconducting Single-Walled Carbon Nanotubes. *Nano Lett.* **2005**, *5* (8), 1621−1624.
(53) Wegner, F. Inverse Participation Ratio in 2 + e Dimensions. *Z. Phys. B: Condens. Matter Quanta* **1980**, *36* (3), 209−214.
(54) Murphy, N. C.; Wortis, R.; Atkinson, W. A. Generalized Inverse Participation Ratio as a Possible Measure of Localization for Interacting Systems. *Phys. Rev. B* **2011**, *83* (18), 184206.
(55) Gifford, B. J.; Sifain, A. E.; Htoon, H.; Doorn, S. K.; Kilina, S.; Tretiak, S. Correction Scheme for Comparison of Computed and Experimental Optical Transition Energies in Functionalized Single-Walled Carbon Nanotubes. *J. Phys. Chem. Lett.* **2018**, *9* (10), 2460−2468.
(56) Wu, X.; Kim, M.; Qu, H.; Wang, Y. Single-Defect Spectroscopy in the Shortwave Infrared. *Nat. Commun.* **2019**, *10* (1), 2672.
(57) Gifford, B.; Saha, A.; Weight, B.; He, X.; Ao, G.; Zheng, M.; Htoon, H.; Kilina, S.; Doorn, S.; Tretiak, S. Mod(n-m,3) Dependence of Defect-State Emission Bands in Aryl- Functionalized Carbon Nanotubes. *Nano Lett.* **2019**, *19* (12), 8503−8509.

https://dx.doi.org/10.1021/acs.jpcc.0c10157
J. Phys. Chem. C 2021, 125, 4785−4793